UC Irvine
UC Irvine Previously Published Works

Title

A finite volume SOFC model for coal-based integrated gasification fuel cell system analysis

Permalink

Journal

ISBN

Authors

Li, M
Brouwer, J
Powers, JD
et al.

Publication Date

DOI

Copyright Information

Peer reviewed

A Finite Volume SOFC Model for Coal-Based Integrated Gasification Fuel Cell Systems Analysis

Mu Li

James D. Powers

Jacob Brouwer[1]
e-mail: jb@nfcrc.uci.edu

Advanced Power and Energy Program,
University of California,
Irvine, CA 92697-3550

Integrated gasification fuel cell (IGFC) systems combining coal gasification and solid oxide fuel cells (SOFC) are promising for highly efficient and environmentally friendly utilization of coal for power production. Most IGFC system analyses performed to-date have used nondimensional thermodynamic SOFC models that do not resolve the intrinsic constraints of SOFC operation. In this work a quasi-two-dimensional (2D) finite volume model for planar SOFC is developed and verified using literature data. Special attention is paid to making the model capable of supporting recent SOFC technology improvements, including the use of anode-supported configurations, metallic interconnects, and reduced polarization losses. Activation polarization parameters previously used for high temperature electrolyte-supported SOFC result in cell performance that is much poorer than that observed for modern intermediate temperature anode-supported configurations; thus, a sensitivity analysis was conducted to identify appropriate parameters for modern SOFC modeling. Model results are shown for SOFC operation on humidified H_2 and CH_4 containing syngas, under coflow and counterflow configurations; detailed internal profiles of species mole fractions, temperature, current density, and electrochemical performance are obtained. The effects of performance, fuel composition, and flow configuration of SOFC performance and thermal profiles are evaluated, and the implications of these results for system design and analysis are discussed. The model can be implemented not only as a stand-alone SOFC analysis tool, but also a subroutine that can communicate and cooperate with chemical flow sheet software seamlessly for convenient IGFC system analysis. [DOI: 10.1115/1.4000687]

Keywords: SOFC, planar, coal gasification, IGFC, finite volume model

1 Introduction

Solid oxide fuel cells (SOFCs) operating at elevated temperatures (873–1273 K) hold the promise of power generation with higher efficiency and lower pollution. Due to high efficiency, high temperature operation, solid state design, and the potential for internal reforming of gaseous fuels, SOFC are ideal for stationary applications. Integrated gasification fuel cell (IGFC) systems that combine SOFC with gasifiers are expected to provide more efficient and environmentally viable utilization of coal, the most abundant fossil fuel resource around the world. Systems analyses have been performed to investigate and optimize IGFC systems with various configurations [1–4]. Most of these analyses have employed "black box" modeling of the SOFC reactor based on thermodynamic analysis and global mass/energy balances. Such models, however, are not capable of revealing many intrinsic constraints to SOFC operation (for example, temperature and current density profiles) and challenges of integrating fuel cell stacks with the gasifier and balance of plant.

Various models [5–9] have been developed to provide more detailed insight into SOFC operation: finite difference and finite element are the most common modeling approaches employed. As an integral form of finite difference discretization, the finite volume method has reasonable accuracy and relatively lighter computational expense, which has also led to its use in SOFC model-

ing [10–12]. The lower computational expense of the finite volume method is critical to its selection in the current work that is aimed at model development for use in detailed systems analyses.

This work discusses the definition and development of a quasi-two-dimensional (2D) finite volume SOFC model that: (1) is based on detailed electrochemical analyses and internal heat transfer calculations; (2) can give not only fuel cell overall performance but also internal profiles of temperature, current density, flow compositions, etc., so that more detailed characteristics of SOFC under different system configurations can be investigated; (3) has short calculation time and the flexibility to be linked to power system analysis tools. Special attention was paid to making the model capable of reflecting some recent developments in the SOFC community such as direct internal reforming (DIR), anode-supported geometry, and the use of metallic interconnects. A planar SOFC geometry was considered due to its higher current/power density and lower fabrication cost, but the approach can also be adapted for tubular or other geometries.

2 Model Description

2.1 Model Features. Only the two parallel-flow configurations (coflow and counterflow) were considered in this work because: (1) the two configurations are sufficiently representative for the purposes of system analysis; (2) the cross-flow configuration requires at least a full-2D model to resolve the geometry, while the parallel-flow configurations can be analyzed through a quasi-2D model, which is more computationally economic. Thus, the finite volume SOFC model represents the most centered channel in the centered cell layer in a fuel cell stack. The structures of
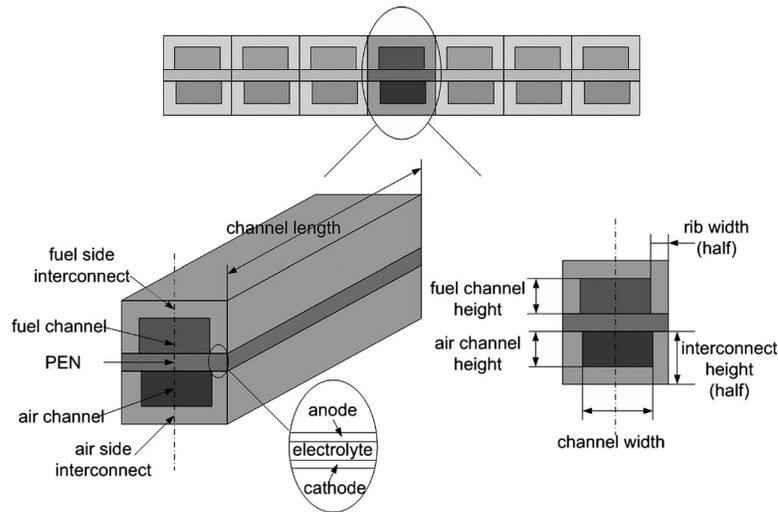

Fig. 1 Fuel cell geometry for coflow and counterflow configurations

fuel flow channel, air flow channel, positive-electrolyte-negative structure (PEN) (which includes the two porous electrodes and the dense solid electrolyte layer), air- and fuel-side interconnects (including rib structures) are resolved. The geometric configuration of the model is shown in Fig. 1.

Figure 2 shows the discretization of the fuel cell channel into a user-defined number of control volumes. Each control volume contains separate temperatures for the fuel channel, air channel, PEN, and interconnects (by applying symmetric boundary conditions, the temperatures of fuel- and air-side interconnects are assumed the same). Campanari and Iora [12], in similar finite volume modeling work, investigated the differences between a "coarse" grid (where the PEN temperature and interconnect temperatures were lumped together as a solid temperature) and a "refined" grid (where fuel- and air-side interconnects were further divided into three control volumes of different temperatures, respectively) and concluded that for parallel-flow configurations, the two different approaches yielded very similar thermal profiles and the differences in terms of total cell balances were within 0.3%. Although it seems well justified to adopt the "coarse" grid in this work to save computational expense, further investigation reveals that at least one independent interconnect temperature should be retained to account for metallic interconnects, which have thermal conductivities at least one order of magnitude greater than that of the PEN.

The model requires the following input information:

(1) cell geometry parameters (fuel and air channel dimensions, solid layer thickness, interconnect rib width, etc.)

(2) inlet fuel and air thermodynamic properties (temperature and pressure) and chemical compositions
(3) desired working voltage or desired average working current density (depending on the calculation option chosen)

The model generates the following information:

(1) overall cell performance: fuel and air utilization, total power output, heat loss by radiation at the edges, average working current density, or working voltage (depending on the calculation option chosen), etc.
(2) internal profiles of various properties: temperature, local current density (power density), local chemical species mole fractions, local electrochemical loss terms, etc.

Two calculation options are available for the model.

(1) The desired working voltage of the fuel cell is given and the model will calculate the average working current density in a straightforward manner.
(2) The desired average working current density is given and the model will calculate iteratively based upon trial working voltage values until a value that satisfies the working current density requirement is found.

2.2 Simplifications and Assumptions. The following simplifications and assumptions are made for the model.

(1) Steady state.
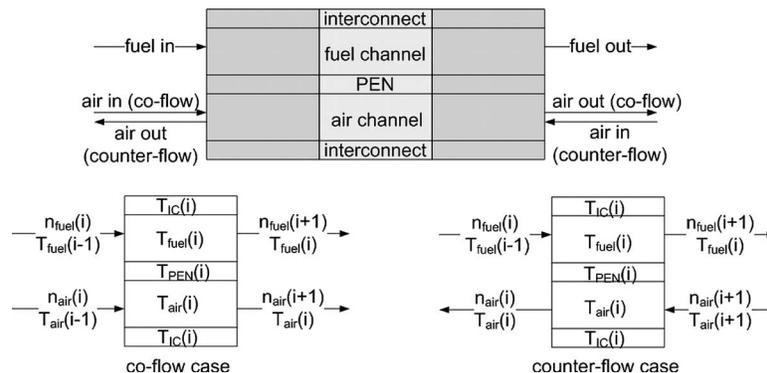(2) The fuel may contain any combination of H_2, CH_4, CO,

Fig. 2 Discretization of calculation domain (coflow and counterflow)

CO_2, H_2O, N_2, and Ar, while air is considered to be comprised of O_2, N_2, CO_2, H_2O, and Ar. Contaminants generally present in coal gasification products, such as tars, particulate matter, nitrogen-containing compounds, and sulfur, are expected to be reduced to sufficiently low concentrations in the syngas that they do not affect the SOFC performance [13].

(3) Each control volume has uniform species concentrations within the fuel and air channels.

(4) Interconnects are treated as equipotential plates due to their high electrical conductivity.

(5) The water gas shift reaction occurs inside the fuel flow channel and is always in an equilibrium state. The equilibrium constant is determined by the local fuel temperature.

(6) Electrochemical oxidation of H_2 occurs at the anode-electrolyte interface, with the reaction kinetics controlled by the local PEN temperature.

(7) The kinetics of CO oxidation at the fuel cell anode is slow compared with H_2 oxidation. Only H_2 participates in electrochemical reactions, while CO is oxidized through the water gas shift reaction. Li and Chyu [14] showed that electrochemical oxidation of both CO and H_2 at the anode yields the same Nernst potential in a SOFC, as long as chemical equilibrium of the shift reaction is attained.

(8) Internal reformation of CH_4 is kinetically limited and occurs at the fuel-anode interface, with the reaction kinetics determined by the local PEN temperature.

(9) 100% of the surface area under the interconnect rib is active for H_2 oxidation but inactive for CH_4 reformation [5].

(10) The Peclet number is large: thus it is reasonable to neglect axial diffusion effects (thermal and mass diffusion) in the gas phases [7].

(11) Radiation heat transfer by gas emission is assumed negligible. Radiation heat transfer between PEN and interconnect in a single control volume was found to be very small due to the small temperature difference. Radiation heat transfer among solids of different control volumes (which may have a larger temperature difference) are also neglected due to small view factors.

(12) Heat loss from the edges of the channel occurs only by radiation. The edge of the fuel cell stack is modeled as a gray surface positioned in a large cavity. The environment (stack chamber) temperature is an input parameter controlled by the model user.

3 Model Equations

3.1 Electrochemical Model. The fuel cell working voltage is calculated as a function of working current density by:

$$V_{cell} = V_{Nernst} - \eta_{act} - \eta_{ohm} - \eta_{dif} = f(j) \tag{1}$$

where V_{cell} is the fuel cell working voltage, V_{Nernst} is the Nernst potential, η is the loss term, and j is the local working current density.

3.1.1 Nernst Potential. The Nernst potential V_{Nernst} is calculated according to the Nernst equation [15]:

$$V_{Nernst} = E^0 + \frac{R_u T_{PEN}}{2F}\left[\ln\left(\frac{x_{H_2}^b (x_{O_2}^b)^{1/2}}{x_{H_2O}^b}\right) + 0.5 \ln\left(\frac{p_{cat}}{p_{amb}}\right)\right] \tag{2}$$

where E^0 is the ideal potential of H_2 oxidation at ambient pressure, as a function of fuel cell reaction site temperature, T_{PEN} is the local PEN temperature, x_i is the local mole fraction of species i, and p is pressure. The value of E^0 is related to the change in Gibbs free energy for H_2 reaction with O_2 to produce H_2O at the operating temperature. E^0 is calculated according to a linear fit of JANAF thermochemical table data [16] for Gibbs free energy in the temperature range of 800–1400 K, which is a typical operating temperature range for SOFC, as follows:

$$E^0 = 1.28628053 - 2.8873 \times 10^{-4} T_{PEN} \tag{3}$$

3.1.2 Activation Polarization. The activation polarization is estimated as the sum of activation polarization at each electrode-electrolyte interface

$$\eta_{act} = \eta_{act}^{an}(j) + \eta_{act}^{cat}(j) \tag{4}$$

The governing equation for the activation polarization is the general Butler–Volmer (BV) equation

$$j = j_0\left[\exp\left(\frac{\alpha n F \eta_{act}}{R_u T_{PEN}}\right) - \exp\left(-\frac{(1-\alpha)n F \eta_{act}}{R_u T_{PEN}}\right)\right] \tag{5}$$

The full B-V equation must be solved implicitly for the activation polarization, whereas in modeling it is often desirable to have the polarization term expressed explicitly as a function of current density. Noren and Hoffman [17] compared several types of explicit approximations and concluded that the hyperbolic sine approximation is recommended:

$$\eta_{act} = \frac{R_u T_{PEN}}{\alpha n F}\sinh^{-1}\left(\frac{j}{2j_0}\right) \tag{6}$$

The exchange current density j_0 can be expressed as an Arrhenius law function of the composition of the reacting species:

$$j_{0,an} = \gamma_{an}\left(\frac{p_{H_2}}{p_{amb}}\right)\left(\frac{p_{H_2O}}{p_{amb}}\right)\exp\left(-\frac{E_{act,an}}{R_u T_{PEN}}\right) \tag{7}$$

$$J_{0,cat} = \gamma_{cat}\left(\frac{p_{O_2}}{p_{amb}}\right)^{0.25}\exp\left(-\frac{E_{act,cat}}{R_u T_{PEN}}\right) \tag{8}$$

Various values for the pre-exponential factor and activation energy of Eqs. (7) and (8) are reported in the literature [8,11–13]. Values reported by Campanari and Iora [12] and Costamagna et al. [8] for simulating an electrolyte-supported SOFC are used in this work for model verification. Note that Hernández-Pacheco et al. [13] clarified that the value of n in Eq. (6) should be 1 (in terms of an individual electron transferred) rather than 2 (number of electrons transferred per oxygen ion).

3.1.3 Ohmic Polarization. It is assumed that the electric current flow path is perpendicular to the SOFC plane. Current flows across interconnects, anode, electrolyte, and cathode under the cell potential difference. The overall ohmic polarization is divided into losses due to resistance of the fuel-side interconnect, PEN, and air-side interconnect:

$$\eta_{ohm} = i(R_{PEN} + R_{IC,fuel} + R_{IC,air}) \tag{9}$$

The resistance of the PEN structure R_{PEN} is calculated by:

$$R_{PEN} = \sum_{k=an,cat,ele} \frac{\rho_k \delta_k}{A_k} \tag{10}$$

where A_k is the area of the section where current flows; δ_k is the corresponding current flow length and is equal to the thickness of the corresponding layer based on the assumptions mentioned above. The temperature dependent material electrical resistivity, ρ_k, of anode, cathode, and electrolyte are calculated according to equations listed in Table 1, cited from the International Energy Agency (IEA) sponsored steady-state modeling benchmark for planar SOFC [18].

For ceramic interconnects whose electrical resistance is comparable to that of PEN, a method presented by Selimovic [10] is adopted in this work. The "L-shaped" interconnect is divided into three rectangular parts, I, II, and III, as shown in Fig. 3.

For part I and II, the electrical resistance values are calculated according to Ohm's law:

$$R_I = \frac{\rho_{IC}a}{\Delta x(c-b)} \tag{11}$$

Table 1 Summary of model parameters

Methane reformation reaction	
Pre-exponential factor K_{rx}	4274 mol s^{-1} m^{-2} bar^{-1}
Coefficient α	1
Coefficient β	0
Activation energy $E_{act,rx}$	82,000 J mol^{-1}
Activation polarization	
Pre-exponential factor for anode	
γ_{an}	5.5×10^8 A m^{-2}
Activation energy for anode $E_{act,an}$	100,000 J mol^{-1}
Pre-exponential factor for cathode	
γ_{cat}	7×10^8 A m^{-2}
Activation energy for cathode	
$E_{act,cat}$	120,000 J mol^{-1} [8]
	117,000 J mol^{-1} [12]
Ohmic polarization	
Specific resistivity of anode	$\left[\dfrac{95 \times 10^6}{T_{PEN}}\exp\left(-\dfrac{1150}{T_{PEN}}\right)\right]^{-1}$ Ω m
Specific resistivity of cathode	$\left[\dfrac{42 \times 10^6}{T_{PEN}}\exp\left(-\dfrac{1200}{T_{PEN}}\right)\right]^{-1}$ Ω m
Specific resistivity of electrolyte	$\left[3.34 \times 10^4 \exp\left(-\dfrac{10,300}{T_{PEN}}\right)\right]^{-1}$ Ω m
Specific resistivity of interconnect	$\left[\dfrac{9.3 \times 10^6}{T_{IC}}\exp\left(-\dfrac{1,100}{T_{IC}}\right)\right]^{-1}$ Ω m
Diffusion polarization	
Porosity of anode	50%
Tortuosity of anode	3.0
Pore diameter of anode	1×10^{-6} m
Porosity of cathode	50%
Tortuosity of cathode	3.0
Pore diameter of cathode	1×10^{-6} m
Diffusion volume of H_2 molecule	6.12
Diffusion volume of H_2O molecule	13.1
Diffusion volume of O_2 molecule	16.3
Diffusion volume of N_2 molecule	18.5
Thermal conductivity	
PEN structure	2 W m^{-1} K^{-1}
Ceramic interconnect	2 W m^{-1} K^{-1}
Metallic interconnect	25 W m^{-1} K^{-1}

$$R_{II} = \frac{\rho_{IC}(d-a)}{\Delta x(c-b)} \tag{12}$$

where Δx represents the length of a control volume along the cell length direction.

For part III an empirical function is employed:

$$R_{III} = \frac{\rho_{IC}}{\Delta x} f\left(\frac{b}{d-a}\right) \tag{13}$$

where the function f takes into account the nonuniformity of the current density distribution inside element III
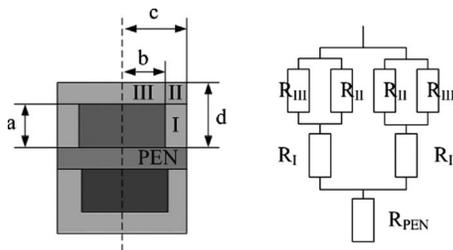

Fig. 3 Electrical resistance of ceramic interconnects

$$f\left(\frac{b}{d-a}\right) = \frac{1}{0.41\left[1-\exp\left(-1.2\dfrac{b}{d-a}\right)\right]} \tag{14}$$

The effective electrical resistance of fuel-side interconnects can be expressed as

$$R_{IC,fuel} = 0.5\left(R_I + \frac{R_{II}R_{III}}{R_{II} + R_{III}}\right) \tag{15}$$

The effective electrical resistance of the air-side interconnect can be calculated in a similar manner.

For metallic interconnects, the electrical resistance of the material itself is so small that it can be neglected. However, it is necessary to take into account the electrical resistance of the oxide scale that grows on these interconnects. In this work, data for Crofer 22 APU are used [19].

3.1.4 Diffusion Polarization. In close proximity to the PEN reaction sites, the concentrations of reactants and products participating in the electrochemical reactions can differ significantly from bulk gas stream concentrations. This effect is related to mass transport by diffusion through the electrodes and results in diffusion polarization, which can be estimated as:

$$\eta_{dif} = \eta_{dif}^{an} + \eta_{dif}^{cat} = \frac{R_u T_{PEN}}{2F}\ln\left(\frac{x_{H_2}^b x_{H_2O}^r}{x_{H_2O}^b x_{H_2}^r}\right) + \frac{R_u T_{PEN}}{4F}\ln\left(\frac{x_{O_2}^b}{x_{O_2}^r}\right) \tag{16}$$

where b and r represent bulk and reaction site concentrations, respectively.

By relating the diffusive flow of H_2, H_2O, and O_2 to the electric current density j through the Faraday's law and assimilating multicomponent diffusion to binary diffusion where necessary, the mole fractions of H_2, H_2O, and O_2 at the reaction sites can be calculated by the following equations [8,11,20]:

$$x_{H_2}^r = x_{H_2}^b - \frac{jR_u T_{PEN}\delta_{an}}{2Fp_{an}D_{an,eff}} \tag{17}$$

$$x_{H_2O}^r = x_{H_2O}^b + \frac{jR_u T_{PEN}\delta_{an}}{2Fp_{an}D_{an,eff}} \tag{18}$$

$$x_{O_2}^r = 1 + (x_{O_2}^b - 1)\exp\left(\frac{jR_u T_{PEN}\delta_{cat}}{4Fp_{cat}D_{cat,eff}}\right) \tag{19}$$

The effective diffusivities at the anode and cathode sides are [20]:

$$D_{an,eff} = \left(\frac{p_{H_2O}}{p_{an}}\right)D_{H_2,eff} + \left(\frac{p_{H_2}}{p_{an}}\right)D_{H_2O,eff} \tag{20}$$

$$D_{cat,eff} = D_{O_2,eff} \tag{21}$$

Since both ordinary diffusion and Knudsen diffusion occur simultaneously, the overall effective diffusivity for H_2, H_2O, and O_2 in porous electrodes can be determined from [8,20]:

$$D_{1,eff} = \frac{\varepsilon}{\tau}\left(\frac{1}{D_{12}} + \frac{1}{D_{K1}}\right)^{-1} \tag{22}$$

where ε and τ are the porosity and tortuosity of the electrode materials, respectively.

The binary diffusivity D_{12} is estimated using the Fuller equation [21]:

$$D_{12} = \frac{0.00143 T_{PEN}^{1.75}}{pM_{12}^{1/2}\left[(\Sigma v)_1^{1/3} + (\Sigma v)_2^{1/3}\right]^2} \tag{23}$$

where $M_{12} = 2[(1/M_1) + (1/M_2)]^{-1}$ and M_i is the molecular weight of species i; $(\Sigma v)_i$ is the diffusion volume of species i.

The Knudsen diffusivity [22] is estimated as:

$$D_{K1} = 48.5 d_{\text{pore}} \left(\frac{T_{\text{PEN}}}{M_1} \right)^{1/2} \qquad (24)$$

where d_{pore} is the diameter of the pore structure and M_1 is the molecular weight of the species.

3.1.5 Water Gas Shift Reaction. The CO in the fuel gas is converted into H_2 by the water gas shift reaction

$$CO + H_2O = H_2 + CO_2 \qquad (25)$$
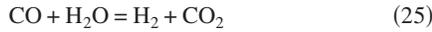
This reaction is assumed fast, such that the species are always in local equilibrium, with the equilibrium constant depending only on the local fuel temperature [11]:

$$K_{p,\text{shift}} = \frac{p_{H_2} p_{CO_2}}{p_{H_2O} p_{CO}} = \frac{x_{H_2} x_{CO_2}}{x_{H_2O} x_{CO}} = \exp\left(\frac{4276}{T_{\text{fuel}}} - 3.961 \right) \qquad (26)$$

3.1.6 Methane Reformation Kinetics. In the SOFC, CH_4 is converted to H_2 and CO in the SOFC by steam reformation, an endothermic reaction that is catalyzed by the nickel/zirconia cermet anode materials.

$$CH_4 + H_2O \rightarrow 3H_2 + CO \qquad (27)$$

Modeling of this methane reformation reaction is based on a chemical kinetic approach. The expression for the molar reaction rate of CH_4 (mol s^{-1}) follows the empirical approach of Achenbach [23]:

$$r_{\text{rx}} = \gamma_{\text{rx}} p_{CH_4}^\alpha p_{H_2O}^\beta \exp\left(-\frac{E_{\text{act,rx}}}{R_u T_{\text{PEN}}} \right) A_{\text{rx}} \qquad (28)$$

where A_{rx} is the reformation reaction surface of the discretized control volume (not including the surface area under the rib); the values of other parameters are listed in Table 1.

3.2 Species Conservation. The overall mole balances for the ith control volume in the fuel and air channels are

$$n_{H_2}(i+1) = n_{H_2}(i) - r_{\text{ele}} + 3r_{\text{rx}} + \Delta n_{H_2}^{\text{shift}} \qquad (29a)$$

$$n_{H_2O}(i+1) = n_{H_2O}(i) + r_{\text{ele}} - r_{\text{rx}} - \Delta n_{H_2O}^{\text{shift}} \qquad (29b)$$

$$n_{CO}(i+1) = n_{CO}(i) + r_{\text{rx}} - \Delta n_{CO}^{\text{shift}} \qquad (29c)$$

$$n_{CO_2}(i+1) = n_{CO_2}(i) + \Delta n_{CO_2}^{\text{shift}} \qquad (29d)$$

$$n_{CH_4}(i+1) = n_{CH_4}(i) - r_{\text{rx}} \qquad (29e)$$

$$n_{O_2}(i+1) = n_{O_2}(i) \mp \frac{1}{2} r_{\text{ele}} \quad (\text{``}-\text{''} \text{ for coflow, ``}$$

$$+\text{'' for counterflow}) \qquad (29f)$$

$$n_{N_2(i+1)} = n_{N_2}(i) \qquad (29g)$$

$$n_{Ar}(i+1) = n_{Ar}(i) \qquad (29h)$$

where r_{ele} stands for the rate of electrochemical oxidation of H_2 and can be related to electric current density through Faraday's law:

$$r_{\text{ele}} = \frac{jA_{\text{ele}}}{2F} \qquad (30)$$

r_{rx} is the methane reformation reaction rate given by Eq. (28), and Δn^{shift} represents the molar change of species due to the water gas shift reaction.

All reaction rates are estimated based on the flow compositions at the fuel inlet edge of each control volume. In a coflow configuration, the flow compositions at all control volumes can be calcu-

lated node by node explicitly; while in a counterflow configuration, iteration is required to determine the correct O_2 outlet flow rates that satisfy mass conservation.

3.3 Energy Conservation. Fuel flow energy conservation takes into account the convective heat transfer with the PEN and the interconnect, as well as the heat exchange with the PEN due to electrochemical and reformation reactions. The following integral form of the energy conservation equation can be obtained

$$\sum_k n_k(i) h_k(i-1) - \sum_k n_k(i+1) h_k(i) + K_{\text{fuel}} A_{\text{fuel-PEN}} (T_{\text{PEN}}(i)$$
$$- T_{\text{fuel}}(i)) + K_{\text{fuel}} A_{\text{fuel-IC}} (T_{\text{IC}}(i) - T_{\text{fuel}}(i)) - r_{\text{rx}} h_{CH_4}(i)$$
$$- r_{\text{rx}} h_{H_2O}(i) + r_{\text{rx}} h_{CO}'(i) + 3 r_{\text{rx}} h_{H_2}'(i) - r_{\text{ele}} h_{H_2}(i) + r_{\text{ele}} h_{H_2O}'(i)$$
$$= 0 \qquad (31)$$

where k is H_2, CH_4, CO, CO_2, H_2O, N_2, and Ar.

It is assumed that for both reformation of CH_4 and electrochemical oxidation of H_2, the reactants are at the fuel (or air) temperature while the products are at the PEN temperature; thus, h is determined based on local fuel (or air) temperature, while h' is determined based on local PEN temperature.

Similarly, the air flow energy conservation equation is

$$\sum_k n_k(i) h_k(i-1) - \sum_k n_k(i+1) h_k(i) + K_{\text{air}} A_{\text{air-PEN}} (T_{\text{PEN}}(i)$$
$$- T_{\text{air}}(i)) + K_{\text{air}} A_{\text{air-IC}} (T_{\text{IC}}(i) - T_{\text{air}}(i)) - \frac{1}{2} h_{O_2}(i) = 0 \qquad (32)$$

where k is O_2, N_2, CO_2, H_2O, and Ar.

K_{fuel} and K_{air} are the convective heat transfer coefficients, calculated from local Nusselt numbers obtained from empirical expressions, and A is the area involved in the convective heat transfer process.

The energy conservation equation for the PEN accounts for heat conduction in axial direction (along the cell length), as well as between the PEN and interconnects (modeled by Fourier's law), convective heat transfer between the PEN and the fuel and air flows, heat generation (positive or negative) due to electrochemical and reformation reactions, as well as the electric work produced by the cell.

$$\frac{T_{\text{PEN}}(i-1) - T_{\text{PEN}}(i)}{R_{\text{PEN}}} - \frac{T_{\text{PEN}}(i) - T_{\text{PEN}}(i+1)}{R_{\text{PEN}}} + \frac{T_{\text{IC}}(i) - T_{\text{PEN}}(i)}{R_{\text{PEN-IC}}}$$
$$+ K_{\text{fuel}} A_{\text{fuel-PEN}} (T_{\text{fuel}}(i) - T_{\text{PEN}}(i)) + K_{\text{air}} A_{\text{air-PEN}} (T_{\text{air}}(i)$$
$$- T_{\text{PEN}}(i)) - W_{\text{ele}} + r_{\text{rx}} h_{CH_4}(i) + r_{\text{rx}} h_{H_2O}(i) - r_{\text{rx}} h_{CO}'(i)$$
$$- 3 r_{\text{rx}} h_{H_2}'(i) + r_{\text{ele}} h_{H_2}(i) + \frac{1}{2} r_{\text{ele}} h_{O_2}(i) - r_{\text{ele}} h_{H_2O}'(i) = 0 \qquad (33)$$

The energy conservation equation for the interconnect accounts for axial heat conduction, as well as conduction between interconnect and PEN, and convective heat transfer between interconnect and fuel and air flows

$$\frac{T_{\text{IC}}(i-1) - T_{\text{IC}}(i)}{R_{\text{IC}}} - \frac{T_{\text{IC}}(i) - T_{\text{IC}}(i+1)}{R_{\text{IC}}} + \frac{T_{\text{PEN}}(i) - T_{\text{IC}}(i)}{R_{\text{PEN-IC}}}$$
$$+ K_{\text{fuel}} A_{\text{fuel-IC}} (T_{\text{fuel}}(i) - T_{\text{IC}}(i)) + K_{\text{air}} A_{\text{air-IC}} (T_{\text{air}}(i) - T_{\text{IC}}(i))$$
$$= 0 \qquad (34)$$

The fuel and air inlet temperature constitute boundary conditions for the fuel and air energy conservation equations. The boundary conditions for the PEN and interconnect can be either adiabatic or controlled by radiation heat transfer to a chamber environment of fixed temperature, as described in Sec. 2.2.

3.4 Solution Scheme. The fuel cell model consists of two interacting modules: the "species conservation" (SC) module (de-

Cell single channel geometry	
Anode thickness	0.05 mm
Cathode thickness	0.05 mm
Electrolyte thickness	0.15 mm
Bipolar plate thickness	2.50 mm
Rib width	2.42 mm
Material properties	
Thermal conductivity (PEN and IC)	2 W m^{-1} K^{-1}
Anode, cathode, electrolyte, and IC electrical conductivities	Same as listed in Table 1
Operation conditions	
System pressure	1 bar
Periphery conditions	Adiabatic
Inlet temperature (air and fuel)	1173 K
Air ratio (O$_2$ basis)	~8.235
Fuel utilization	85%
Mean current density	3000 A m^{-2}
Inlet gas composition (Benchmark 1)	Fuel: 90% H$_2$; 10% H$_2$O (mole fraction)
	Air: 21% O$_2$; 79% N$_2$ (mole fraction)
Inlet gas composition (Benchmark 2)	Fuel: 26.26% H$_2$, 17.1% CH$_4$, 2.94% CO,
	4.36% CO$_2$, 49.34% H$_2$O (mole fraction)
	Air: 21% O$_2$; 79% N$_2$ (mole fraction)

IEA benchmark defined air ratio as the ratio of actual air molar flow rate to the stoichiometric air molar flow rate that is required to consume all the incoming fuel; the original number based on this definition is 7. The number here is converted to be consistent with the air ratio definition used in this work.

scribed in Sec. 3.2) and the "energy conservation" (EC) module (described in Sec. 3.3). The SC module calculates the chemical species profiles and current density distribution in the fuel cell. These data are then passed as inputs to the EC module, which calculates temperature distribution, heat transfer, and heat loss throughout the fuel cell. The calculation results from the EC module are then passed back as inputs to the SC module for an update. This iterative calculation process repeats until the temperature field difference between two consecutive iterations is smaller than a predefined residual error, at which point the calculation is considered converged.

To improve calculation speed, so that the model can be called within systems analysis tasks, the specific enthalpies of the species, which are typically characterized by high order functions of temperature, are linearized as follows:

$$h_k = a + bT \quad (k = \text{H}_2, \text{CH}_4, \text{CO}, \text{CO}_2, \text{H}_2\text{O}, \text{O}_2, \text{N}_2, \text{Ar}) \quad (35)$$

This simplification is only valid for a reasonably narrow range of temperatures consistent with SOFC operation. With this simplification, the energy conservation equations can be written into four tridiagonal matrices, which can be solved very efficiently by the tridiagonal matrix algorithm (TDMA) [24].

The model can work as a standalone SOFC model or as an integrated user-defined block in chemical flow sheet software (e.g., ASPEN PLUS®). The results presented here were produced by the standalone SOFC model running in MATLAB®. The same model has been implemented in FORTRAN code and successfully linked to ASPEN PLUS® through a user-defined communication interface.

4   Model Verification

The model was verified using the planar SOFC modeling benchmark developed by the IEA [18]. The benchmark contains two cases of SOFC operation: (1) one-cell operation with humidified H$_2$ fuel and ambient air feed and (2) one-cell operation with direct internal steam reformation of CH$_4$ and air. The two cases are designated "Benchmark 1" and "Benchmark 2," respectively; and the operating conditions for the two cases are listed in Table 2.

It is important to clarify the way air ratio is defined in order to make a consistent comparison. In this work, the air ratio is defined as the ratio of actual air molar flow rate to the stoichiometric air molar flow rate that is required to meet the defined fuel utilization

$$\lambda = \frac{\left(\dfrac{n_{\text{air}}}{n_{\text{fuel}}}\right)_{\text{actual}}}{u_f \left(\dfrac{n_{\text{air}}}{n_{\text{fuel}}}\right)_{\text{stoich}}} \quad (36)$$

Some sources (including the IEA Benchmark) use a different definition, and these values have been converted appropriately here.

As stated previously, the parameters for activation polarization vary among different literature sources. For verification, the data sets used by Campanari and Iora [11] (Calculation I) and Costamagna et al. [8] (Calculation II) were both tested and the simulation results from these tests are listed in Tables 3 and 4.

For Benchmark 1, the performance predicted by this model closely agrees with the benchmark performance. For Benchmark 2 the model predicts a slightly lower voltage than the benchmark results. The discrepancy is likely related to activation and diffusion polarization parameters that differ from those used in the IEA Benchmark.

Table 3   Model verification results for IEA Benchmark 1

Parameter	Benchmark 1	Calculation I	Calculation II
Voltage (V)	High/low		
	0.722/0.702	0.715	0.704
Current density (A m^{-2})	High/low		
Max	3957/3725	3961	3780
Min	1366/1020	977	1190
PEN temperature (K)	High/low		
Max	1371/1321	1333	1337
Min	1203/1182	1190	1189
Outlet gas temperature (K)	High/low		
Air	1340/1321	1332	1335
Fuel	1341/1321	1333	1337

Table 4 Model verification results for IEA Benchmark 2

Parameter	Benchmark 2	Calculation I	Calculation II
Voltage (V)	High/low		
	0.649/0.633	0.626	0.607
Current density (A m^{-2})	High/low		
Max	3665/3040	3686	3718
Min	2508/1748	1663	1586
PEN temperature (K)	High/low		
Max	1307/1294	1298	1304
Min	1135/1120	1120	1120
Outlet gas temperature (K)	High/low		
Air	1299/1289	1296	1301
Fuel	1299/1294	1298	1304

Table 6 Model results for intermediate temperature anode-supported SOFC using literature parameters (cell operating at 0.7 V, fuel utilization=0.85, and air utilization=0.14)

	Coflow case	Counterflow case
Average current density (A cm^{-2})	0.14	0.14
Average power density (W cm^{-2})	0.095	0.095
Average anode side activation loss ($\times 10^{-3}$ V)	77.5	79.6
Average cathode side activation loss ($\times 10^{-3}$ V)	147.4	139.4
Average ohmic loss ($\times 10^{-3}$ V)	8.9	10.5
Average anode side diffusion loss ($\times 10^{-3}$ V)	2.6	5.0
Average cathode side diffusion loss ($\times 10^{-3}$ V)	0.087	0.14

5 Model Results

5.1 Intermediate Temperature Anode-Supported SOFC Performance. Many developers are now focusing on SOFC that operate at reduced temperatures (823–1123 K), enabling the use of a wider range of materials (especially metallic interconnects) and more cost-effective fabrication. Also, anode-supported SOFCs that minimize ohmic losses through use of a very thin electrolyte are commonly used. In this work, the SOFC model is applied to an intermediate temperature, anode-supported SOFC with metallic interconnects. The fuel cell geometry and operating conditions are listed in Table 5. The cell working voltage is set to 0.7 V (which is reasonable for comparison to recent literature results for SOFCs), and the resulting current and power density distributions are calculated.

Results are listed in Table 6. At these operating conditions, cell performance is poor despite the reduced ohmic resistance. Activation polarizations dominate the losses and far outweigh the ohmic loss, a result that is not consistent with observations of modern SOFCs (e.g., those recently reported by Solid State Energy Conversion Alliance industry teams [25]), where ohmic loss is smaller than activation loss and overall performance is much greater. This indicates that the activation loss parameters used by Campanari and Iora [12] and Costamagna et al. [8] are not appropriate for

state-of-the-art SOFCs operating at intermediate temperatures. Updated activation loss parameters are therefore required. However, such parameters are difficult to obtain because most of the detailed information on materials, microstructure, and properties are proprietary to developers and very rarely can be found in the published literature. Thus, a sensitivity analysis of the activation parameters was conducted to determine appropriate parameters for predicting state-of-the-art intermediate temperature SOFC performance.

SOFC developers have recently shown significant performance improvements compared with literature values. For example, GE has reported a 0.480 W cm^{-2} power density at 0.8 V and 84% fuel utilization operating on simulated high H$_2$ syngas in a single cell at a uniform temperature of 1073 K [25]. Delphi has demonstrated a 0.725 W cm^{-2} power density at 0.8 V for a five-cell stack with fuel containing 48.5% H$_2$ and 3% H$_2$O (balanced by N$_2$) at 1023 K [26]. It is expected that recent developments in SOFC technology would significantly reduce the activation energy for electrode-electrolyte interface charge transfer. Thus the sensitivity analyses vary the activation energies in Eqs. (7) and (8) to identify parameters that can produce performance consistent with recent data from state-of-the-art SOFC. The geometry and operation conditions are the same as those listed in Table 5, except that the operating voltage is increased from 0.7 V to 0.8 V, so that

Table 5 Parameters and operation conditions for intermediate temperature anode-supported SOFC test

Cell single channel geometry	
Channel length	300 mm
Channel width	3 mm
Fuel channel height	1 mm
Air channel height	2 mm
Anode thickness	1 mm
Cathode thickness	0.05 mm
Electrolyte thickness	0.01 mm
Bipolar plate thickness	3.5 mm
Rib width	2.42 mm
Material properties	
Thermal conductivity of PEN	2 W m^{-1} K^{-1}
Thermal conductivity of interconnect	25 W m^{-1} K^{-1}
Anode, cathode, electrolyte conductivities	Same as listed in Table 1
Interconnect resistivity	Negligible
Operation conditions	
System pressure	1 bar
Periphery conditions	Adiabatic
Inlet temperature (air and fuel)	973 K
Air ratio (O$_2$ basis)	7
Fuel utilization	85%
Working voltage	0.7 V
Inlet gas composition	Fuel: 90% H$_2$; 10% H$_2$O (mole fraction)
	Air: 21% O$_2$; 79% N$_2$ (mole fraction)

Table 7 Results of sensitivity analysis (cell operating at 0.8 V, fuel utilization=0.85, and air utilization=0.14)

	Baseline	Test 1	Test 2	Test 3	Test 4
$E_{act,an}$ (kJ mol^{-1})	100	75	50	50	50
$E_{act,cat}$ (kJ mol^{-1})	120	120	120	100	80
Fuel inlet flow rate (10^{-6} mol/s)	7.26	10.33	10.65	57.33	126.6
Average current density (A cm^{-2})	0.066	0.094	0.097	0.52	1.15
Average power density (W cm^{-2})	0.053	0.075	0.077	0.42	0.92
Anode activation ($\times 10^{-3}$ V)	45.1	4.3	0.3	1.5	3.4
Cathode activation ($\times 10^{-3}$ V)	89.0	129.2	133.1	90.9	21.2
Ohmic ($\times 10^{-3}$ V)	4.7	6.9	7.1	42.0	92.0
Anode diffusion ($\times 10^{-3}$ V)	1.4	1.9	2.0	10.2	23.8
Cathode diffusion ($\times 10^{-3}$ V)	0.04	0.06	0.06	0.3	0.8
Fuel outlet temperature (K)	1129	1129	1129	1132	1135
Air outlet temperature (K)	1129	1129	1129	1129	1129

recent improvements can be better simulated.

For modern SOFC, very small anode side activation losses, on the order of several mV, are expected. Cathode side activation losses, on the other hand, are generally higher and are expected to be on the order of 100 mV, while ohmic losses lie somewhere between. The results of the sensitivity analyses are listed in Table 7. Note that Test 3 achieves reasonable SOFC performance with the various loss terms in the expected range. Thus, the Test 3 parameters have been used in all subsequent analyses.

5.2 SOFC Performance on Humidified H$_2$ Fuel. Using parameters obtained from the sensitivity analysis, an anode-supported SOFC operated at intermediate temperature was simulated. The model is designed to be used for coal-based IGFC system analyses; however, syngas compositions can vary significantly depending upon the various gasification and gas cleanup processes that can be employed. Fortunately, the two gas compositions used in the IEA benchmark (Table 2) can be thought of as representative of the two categories that are of great interest to IGFC operation with CO$_2$ separation and thus can still be employed here for consistency and simplicity. The humidified H$_2$ case is representative of syngas after water gas shift reaction followed by CO$_2$ capture; the second case, containing about 17% (mole fraction) CH$_4$, is consistent with recent growing interest in employing direct internal reformation in SOFC operation coupled with lower temperature gasification for better heat integration.

The model predicts profiles of species mole fractions, temperatures, and all electrochemistry-related variables. Figures 4 and 5 present results for a SOFC operating on humidified H$_2$ (the Benchmark 1 composition indicated in Table 2) in a coflow configuration.

Figure 4(a) presents the mole fraction profiles along the cell length of the gas species in the fuel channel. As expected, the H$_2$ mole fraction decreases and H$_2$O mole fraction increases along

the flow direction. Figure 4(b) shows the temperature distribution along the cell length. All four temperatures increase monotonically along the flow direction. Fuel, PEN, and interconnect temperatures are very close to each other, while the air temperature is consistently lower. This is reasonable since, in this case, the air is the major sink for the heat generated by the electrochemical reactions. The slope of temperature increase is smaller at the fuel and air exit due to the slower hydrogen electrochemical oxidation (smaller local current density).

Profiles of current density, the Nernst potential, and various electrochemical loss terms are presented in Fig. 5. The Nernst potential decreases monotonically along the flow direction due to the temperature increase and reactant consumption. The current density peaks at about 1/3 of the channel length from the fuel inlet edge. This is because although the Nernst potential decreases monotonically along the cell length, the increasing temperature improves reaction rates and reduces some polarization terms (e.g., activation and ohmic polarization). Further downstream the reduction of polarization is not sufficient to compensate for the loss in Nernst potential, and the local current density begins to drop. The local current density is significantly lower at the fuel exit than at the inlet. As expected, activation polarization is the dominant loss term, followed by ohmic polarization. These results provide insights that are helpful for cell design, for example, by estimating the usefulness of the latter part of the channel or determining whether or not it is cost-effective to push the fuel utilization in a single pass to a very high level given the very low local current density near the fuel exit edge.

For the coflow geometry and H$_2$ operation, the minimum and maximum fluid temperatures occur at the inlet and outlet of the SOFC, respectively. As a result, the insights provided by a dimensional SOFC model compared with a nondimensional thermodynamic model are useful, but not as consequential. On the other
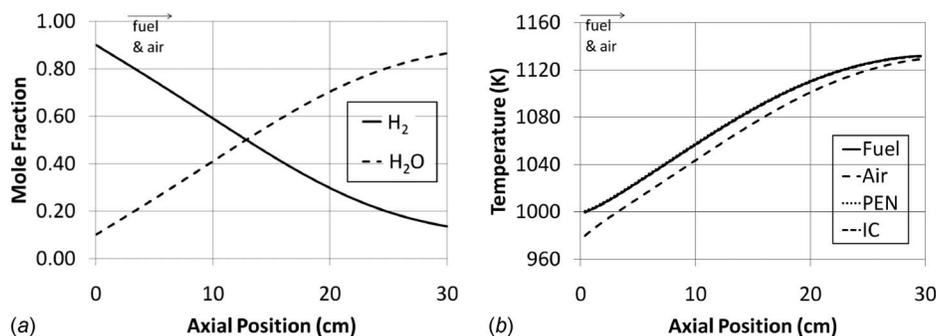

Fig. 4 Fuel channel species mole fractions (a) and temperature distributions (b) along the cell length for humidified H$_2$, coflow operation
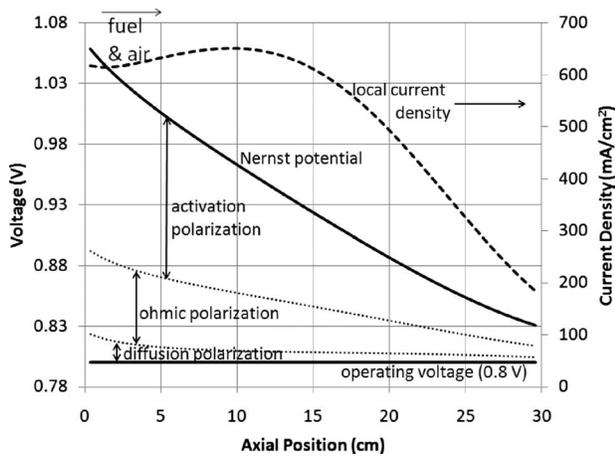
Fig. 5 Predicted working voltage, current density, and contribution of all the various polarization terms along the cell length for humidified H₂, coflow operation
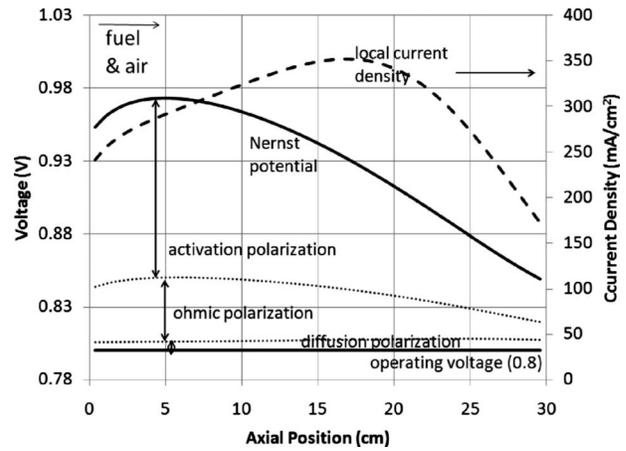

Fig. 7 Predicted working voltage, current density and contribution of all the various polarization terms along the cell length for CH₄ containing syngas, coflow operation

hand, for operation on fuels that contain significant CH_4 concentrations where internal reformation is active, the internal profiles become much more complicated and a thermodynamic model will not generally be sufficient to resolve the conditions. Dimensional models may also be required when considering other cell configurations, like counter- or cross-flow.

For the H_2 fuel counterflow configuration, the predicted trends of H_2 and H_2O mole fractions along the cell length are similar to those of the coflow case. The internal peak temperature is again observed very close to the air outlet, which in this case is the fuel inlet. In the counterflow configuration, the fuel outlet temperature is low (approximating the air inlet temperature), due to the fact that fuel flow does not contribute significantly to heat removal from the cell. The result is a slightly higher air outlet temperature than that predicted for the coflow case (1143 K versus 1129 K in the current example). Also, because the temperatures are highest

at the fuel inlet, where the fuel concentration is also greatest, this case results in a steeper current density distribution and a slightly higher overall power density at a constant cell voltage (0.435 W cm^{-2} versus 0.416 W cm^{-2}). The cell performances for both coflow and counterflow hydrogen cases are listed in Table 8.

5.3 SOFC Performance on CH₄ Containing Fuel With Internal Reformation. Figures 6 and 7 present results for the SOFC operating on CH_4 containing syngas in a coflow configuration. Figure 6(a) presents the mole fraction distributions. Because of methane reformation and water gas shift reaction, the H_2 concentration first increases while the H_2O concentration decreases. CH_4 is completely consumed by about 2/3 of the flow channel. Due to the endothermic methane reformation reaction, there is a temperature dip near the fuel inlet edge, as can be seen in Fig. 6(b). Still the temperature of the fuel, PEN, and interconnect are very close to one another. The air temperature is higher than the PEN (and

Table 8 Summary of SOFC performances using new parameters (cell operating at 0.8 V, fuel utilization=0.85, and air utilization=0.14)

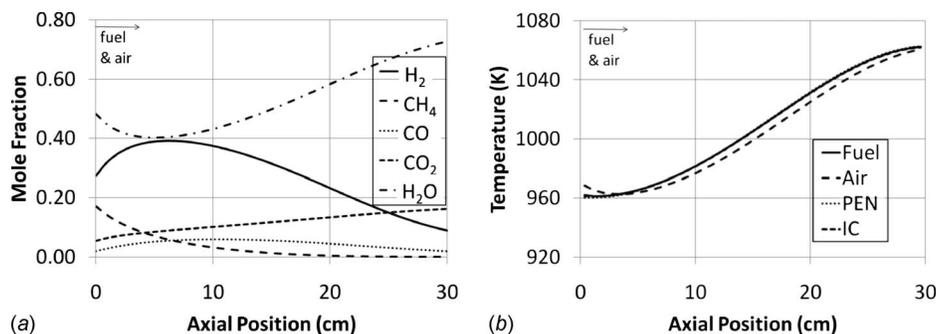|	Coflow		Counterflow	
	Humidified H₂	CH₄ containing	Humidified H₂	CH₄ containing
Average current density (A cm⁻²)	0.52	0.30	0.54	0.42
Average power density (W cm⁻²)	0.42	0.24	0.43	0.33
Peak PEN temperature (K)	1132	1062	1155	1105
Lowest PEN temperature (K)	1001	960	984	987
Fuel outlet temperature (K)	1132	1062	984	987
Air outlet temperature (K)	1129	1061	1143	1071

Fig. 6 Fuel channel species mole fractions (a) and temperature distributions (b) along the cell length for CH₄ containing fuel with internal reformation, coflow operation
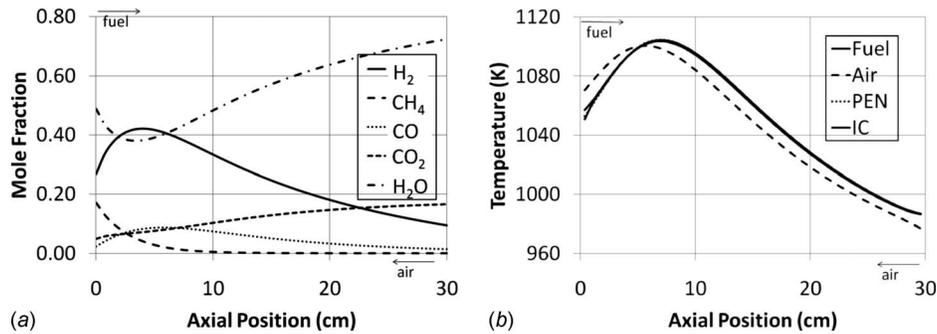
Journal of Fuel Cell Science and Technology

AUGUST 2010, Vol. 7 / **041017-9**

Fig. 8 Fuel channel species mole fractions (*a*) and temperature distributions (*b*) along the cell length for CH_4 containing fuel with internal reformation, counterflow operation

fuel and interconnect) temperature near the inlet because the endothermic reformation reaction causes the PEN to serve as the heat sink in this region.

The current density peaks at a point further down the channel than in the H_2 case, largely because of the cooling and additional H_2 production that results from methane reformation (see Fig. 7). The activation polarization is more significant than that observed for the H_2 case primarily because of the diluting impact of CH_4 and other components in the fuel channel, which reduces the local Nernst potential.

Figures 8 and 9 present SOFC performance with CH_4 containing syngas for the counterflow configuration. The species concentration distributions shown in Fig. 8(*a*) exhibit trends similar to those of the coflow case, except that CH_4 is consumed faster in the counterflow configuration due to the higher temperatures near the fuel inlet. All CH_4 is consumed in the first 1/3 of the cell length; while in the coflow case, CH_4 is more gradually reformed along the fuel channel length. Figure 8(*b*) presents the internal temperature profiles, which are very different from any of the previous cases. The peak temperature position has moved inside the cell, away from the edges, and its magnitude is much greater than that of the inlet and outlet temperatures. The local current density exhibits a distribution that tracks the temperature profile, as can be seen in Fig. 9.

The high internal temperature in the counterflow case results from rapid methane reformation at the fuel inlet producing a very high local H_2 concentration. The H_2 is in-turn consumed very rapidly at the high local temperatures, causing the local current density to spike to nearly 0.7 A cm^{-2}, approximately double the peak current density observed in the coflow case. The resulting

cell power density is 39% greater than in the coflow case, which goes hand in hand with the higher average and peak SOFC temperatures and steep temperature gradients. In the counterflow configuration there are steeper local temperature gradients, either with humidified H_2 or CH_4 containing syngas than in the coflow case. Further, the maximum local cell temperatures can be significantly higher than those observed at either the inlet or the outlet. Aguiar et al. [7] observed similar modeling results using a finite difference model. Steep temperature gradients can lead to thermally induced fractures of SOFC ceramic components, and excessive local temperatures are associated with increased degradation rates. Therefore, it is important to understand and control internal temperature profiles, which are difficult to access experimentally.

From the viewpoint of overall heat balance, CH_4 containing fuel is capable of chemically recovering the heat generated inside the fuel cell channel and has the potential to cool the cell without high air flow. But results obtained in this work reveal that the concurrent processes of endothermic methane reformation and exothermic hydrogen electrochemical oxidation under SOFC operating conditions and with current SOFC materials sets do not necessarily counterbalance locally. The imbalanced local rates of reformation chemistry and electrochemistry lead to temperatures and gradients that are important to resolve and understand and that cannot be observed with a thermodynamic model.

A dimensional model is also needed to clarify the effects of SOFC design on performance. The cell performance for the modeled cases is listed in Table 8. For CH_4 containing fuel, the performance improvement in the counterflow configuration is quite significant and related to the higher average cell temperature. From this point of view, it is preferable to use a counterflow configuration when operating with CH_4 containing syngas, but the internal temperature profiles must be carefully monitored and controlled if this is to be enabled.

6 Summary and Conclusions

A finite volume SOFC model has been developed for coal-based IGFC systems analysis. The model solves species conservation and energy conservation equations, and contains an electrochemical model that accounts for various polarization mechanisms for SOFC operation. The developed model was first verified using IEA benchmark data showing that results well-matched the benchmarks. To overcome the problem that activation loss parameters available in literature cannot well simulate recent SOFC performance in the intermediate temperature range, a sensitivity analysis was conducted to identify a set of parameters that can match modern SOFC performance expectations. The model with new parameters was then used to investigate SOFC performance operating on two types of coal syngas (humidified H_2 and CH_4 containing syngas), under coflow or counterflow configurations. The counterflow configuration can generally produce higher current/power density, but has steeper local temperature gradients that have to be monitored and handled carefully. Except for the
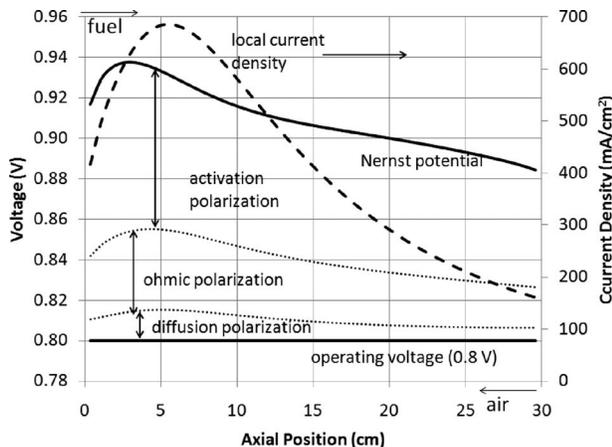

Fig. 9 Predicted working voltage, current density and contribution of all the various polarization terms along the cell length for CH_4 containing syngas, counterflow operation

relatively simple coflow humidified H_2 operation, SOFC operation generally results in complicated internal temperature, species, and current density profiles, which are beyond the resolving ability of a thermodynamic model. These results demonstrate the necessity of employing a detailed dimensional SOFC model in systems analysis to avoid erroneous or misleading conclusions. Future work will apply the developed model in detailed coal-based IGFC systems analysis work to better address the intrinsic constraints for SOFC under various system configurations.

Acknowledgment

Nomenclature

A = area, m^2

$D_{i,\text{eff}}$ = effective diffusivity of species i in porous materials, $m^2\ s^{-1}$

$D_{i,j}$ = binary diffusivity of species i in species j, $m^2\ s^{-1}$

$D_{K,i}$ = Knudsen diffusivity of species i in porous materials, $m^2\ s^{-1}$

E^0 = ideal potential of H_2 oxidization at ambient pressure, V

E_{act} = activation energy, $J\ mol^{-1}$

F = Faraday's constant, $96,485.34\ C\ mol^{-1}$

K = convective heat transfer coefficient, $W\ m^{-2}\ K^{-1}$

K_p = equilibrium constant

M = molecular weight, $kg\ kmol^{-1}$

R = ohmic resistance, Ω, or heat conduction resistance, $W\ K^{-1}$

R_u = universal gas constant, $8.314\ J\ mol^{-1}\ K^{-1}$

T = temperature, K

V = voltage, V

h = specific enthalpy of species, $J\ mol^{-1}$

i = electric current, A

j = electric current density, $A\ m^{-2}$

j_0 = exchange current density, $A\ m^{-2}$

k = thermal conductivity, $W\ m^{-1}\ K^{-1}$

n = number of electrons transferred per reaction or mole flow rate, $mol\ s^{-1}$

p = pressure, bar

r_{rx} = rate of methane reformation reaction, $mol\ s^{-1}$

r_{ele} = rate of electrochemical oxidation of H_2, $mol\ s^{-1}$

u_f = fuel utilization factor

x_i = molar fraction of species i

Greek Symbols

α = electron transfer coefficient or parameter in the methane reformation reaction rate expression

β = parameter in the methane reformation reaction rate expression

γ = pre-exponential factor in exchange current density calculation

δ = thickness, m

η = polarization loss, V

Subscripts

air = air or air-side

amb = ambient conditions

an = anode

cat = cathode

ele = electrolyte or related to electrochemical oxidation of H_2

fuel = fuel or fuel-side

IC = interconnect

PEN = positive-electrolyte-negative structure

rx = methane reformation reaction

shift = water gas shift reaction

Superscripts

an = anode

b = bulk flow

cat = cathode

r = reaction site

References

[1] Kuchonthara, P., Bhattacharya, S., and Tsutsumi, A., 2005, "Combination of Thermo-Chemical Recuperative Coal Gasification Cycle and Fuel Cell for Power Generation," Fuel, **84**(7–8), pp. 1019–1021.

[2] Ghosh, S., and De, S., 2006, "Energy Analysis of a Cogeneration Plant Using Coal Gasification and Solid Oxide Fuel Cell," Energy, **31**(2–3), pp. 345–363.

[3] Rao, A., Verma, A., and Samuelsen, G., 2005, "Engineering and Economic Analyses of a Coal-Fueled Solid Oxide Fuel Cell Hybrid Power Plant," ASME Paper No. GT2005-68762.

[4] Verma, A., Rao, A. D., and Samuelsen, G. S., 2006, "Sensitivity Analysis of a Vision 21 Coal Based Zero Emission Power Plant," J. Power Sources, **158**(1), pp. 417–427.

[5] Braun, R., 2002, "Optimal Design and Operation of Solid Oxide Fuel Cell System for Small Scale Stationary Applications," Ph.D. thesis, University of Wisconsin-Madison, Madison, WI.

[6] Recknagle, K. P., Williford, R. E., Chick, L. A., Rector, D. R., and Khaleel, M. A., 2003, "Three-Dimensional Thermo-Fluid Electrochemical Modeling of Planar SOFC Stacks," J. Power Sources, **113**(1), pp. 109–114.

[7] Aguiar, P., Adjiman, C. S., and Brandon, N. P., 2004, "Anode-Supported Intermediate Temperature Direct Internal Reforming Solid Oxide Fuel Cell. I: Model-Based Steady-State Performance," J. Power Sources, **138**(1–2), pp. 120–136.

[8] Costamagna, P., Selimovic, A., Borghi, M. D., and Agnew, G., 2004, "Electrochemical Model of the Integrated Planar Solid Oxide Fuel Cell (IP-SOFC)," Chem. Eng. J., **102**(1), pp. 61–69.

[9] Mueller, F., Brouwer, J., and Jabbari, F., 2006, "Dynamic Simulation of an Integrated Solid Oxide Fuel Cell System Including Current-Based Fuel Flow Control," ASME J. Fuel Cell Sci. Technol., **3**, pp. 144–154.

[10] Selimovic, A., 2002, "Modeling of Solid Oxide Fuel Cells Applied to the Analysis of Integrated Systems With Gas Turbines," Ph.D. thesis, Lund University, Sweden.

[11] Campanari, S., and Iora, P., 2004, "Definition and Sensitivity Analysis of a Finite Volume SOFC Model for a Tubular Cell Geometry," J. Power Sources, **132**(1–2), pp. 113–126.

[12] Campanari, S., and Iora, P., 2005, "Comparison of Finite Volume SOFC Models for the Simulation of a Planar Cell Geometry," Fuel Cells, **5**(1), pp. 34–51.

[13] Hernández-Pacheco, E., Mann, M. D., Hutton, P. N., Singh, D., and Martin, K. E., 2005, "A Cell-Level Model for a Solid Oxide Fuel Cell Operated With Syngas From a Gasification Process," Int. J. Hydrogen Energy, **30**(11), pp. 1221–1233.

[14] Li, P. W., and Chyu, M. K., 2005, "Electrochemical and Transport Phenomena in Solid Oxide Fuel Cells," ASME J. Heat Transfer, **127**(12), pp. 1344–1362.

[15] Larminie, J., and Dicks, A., 2003, *Fuel Cell Systems Explained*, 2nd ed., Wiley, West Sussex, England.

[16] Chase, M., 1986, *JANAF Thermochemical Tables*, 3rd ed., American Chemical Society, Washington, DC.

[17] Noren, D. A., and Hoffman, M. A., 2005, "Clarifying the Butler–Volmer Equation and Related Approximations for Calculating Activation Losses in Solid Oxide Fuel Cell Models," J. Power Sources, **152**, pp. 175–181.

[18] Achenbach, E., 1996, *SOFC Stack Modeling, Final Report of Activity A2, Annex II: Modeling and Evaluation of Advanced Solid Oxide Fuel Cells*, International Energy Agency, Jüelich, Germany.

[19] ThyssenKrupp VDM, 2008, "Crofer 22 APU, Material Data Sheet No. 4046," Jun. 2008 ed.

[20] Chan, S. H., and Xia, Z. T., 2001, "Anode Micro Model of Solid Oxide Fuel Cell," J. Electrochem. Soc., **148**(4), pp. A388–A394.

[21] Reid, R., Prausnitz, J., and Poling, B., 1987, *The Properties of Gases and Liquids*, 4th ed., McGraw-Hill, New York.

[22] Perry, R., and Green, W., 1997, *Perry's Chemical Engineer's Handbook*, 7th ed., McGraw-Hill, New York.

[23] Achenbach, E., 1994, "Three-Dimensional and Time-Dependent Simulation of a Planar Solid Oxide Fuel Cell Stack," J. Power Sources, **49**(1–3), pp. 333–348.

[24] Patankar, S., 1980, *Numerical Heat Transfer and Fluid Flow*, 1st ed., Hemisphere, Washington, DC.

[25] Surdoval, W., 2007, "The U. S. Department of Energy Fossil Energy Fuel Cell Program Solid State Energy Conversion Alliance Goals and Challenges," Eighth Annual SECA Workshop, San Antonio, TX.

[26] Shaffer, S., 2008, "Delphi SOFC Development Update," Ninth Annual SECA Workshop, Pittsburgh, PA.